Int. J. Electrochem. Sci., 9 **(2014)** 8340 - 8354

International Journal of
ELECTROCHEMICAL
SCIENCE
www.electrochemsci.org

Facile Synthesis of MnO_2/graphene Electrode by Two-steps Electrodeposition for Energy Storage Application

Sameh Hassan[1,3], *Masaaki Suzuki*[2], *Ahmed Abd El-Moneim*[1,4,*]

[1] Materials Science and Engineering Department, Egypt-Japan University of Science and technology, New Borg El Arab City, Alexandria, Egypt, 21934
[2]Department of Chemical Engineering, Tokyo Institute of Technology, 2-12-1 O-okayama, Meguro-ku, Tokyo, Japan, 152-8552
[3]Currently working at Physics Department, Faculty of Science, Menoufiya University, Shebin El Kom, Egypt.
[4] On leave from Physical Chemistry Department, National Research Centre, Cairo, Egypt.
[*]E-mail: ahmed.abdelmoneim@ejust.edu.eg; oneim99@yahoo.com

Received: 2 September 2014 / *Accepted:* 17 October 2014 / *Published:* 28 October 2014

MnO_2/graphene electrode was developed via anodic deposition of nanostructured MnO_2 film on electrophoretically reduced graphene oxide (EPD-rGO) film. The electrodeposited MnO_2, EPD-rGO and MnO_2/EPD-rGO electrodes were characterized and investigated for supercapacitor application using scanning electron microscopy, transmission electron microscopy, X-ray diffraction, fourier transform infrared spectroscopy, cyclic voltammetry, galvanostatic charge/discharge, and electrochemical impedance spectroscopy. The electrophoretic deposition enables the development of rGO film composed of overlapped platelets of defective graphene sheets. The MnO_2/ EPD-rGO electrode shows better specific capacitance and rate capability than MnO_2 electrode; it exhibits specific capacitance of 822 Fg^{-1} and better cyclic stability at a current density of 1 mA cm^{-2}. The large surface area and defective nature of EPD-rGO film in conjunction with an efficient utilization of MnO_2 nanoparticles facilitated rapid ion transport and electrochemical cyclic stability, and hence offering the potential of the unique capacitive behavior. The obtained results indicate electrophoretic deposition could set a facile base for providing graphene-based materials, at room temperature without using harsh and toxic chemicals or high synthesis temperature.

Keywords: Electrophoretic deposition, Manganese dioxide, Supercapacitor, Nickel foam, Graphene.

1. INTRODUCTION

The development of more advanced and environmentally friendly energy storage devices is a pressing requirement to meet future societal and environmental needs. Supercapacitors are one of the

most hopeful electrochemical energy storage devices due to their pulse power supply, long cycle life, and quickly response [1,2]. Many materials have been investigated as possible supercapacitor electrodes including (1) carbon, (2) conducting polymers, and (3) metal oxides [3,4]. Carbon materials exhibit the capacitance arising from the formation of an electrical double layer (EDLC) between the carbon surface and the electrolyte. In contrast to carbon materials, the last two kinds of materials produce a pseudo Faradic reaction which also are provide a pseudocapacitive behavior. Much effort has been devoted to metal oxides for capacitor development because of their large specific capacitance and fast redox kinetics than conducting polymers [5].

Manganese oxide (MnO_2), as a promising electrode material for many catalytic applications in general [6-14] and supercapacitors, in particular, has received considerable interests in virtue of its low cost, high theoretic capacitance (about 1370 F g^{-1}), good cycle stability and environmental friendliness [15,16]. However, the poor electrical conductivity and densely packed structure of MnO_2 limit its application within the development of high performance supercapacitors. Hence, the most important basic challenge to adapt MnO_2-based supercapacitor for commercial application is to improve its energy density, via approaching specific capacitance close to that of its theoretical specific capacitance, while keeping a high power density and a long cycle life. To optimize electrochemical performance of MnO_2-based electrodes, considerable research efforts have been placed on exploring hybrid composite structures where MnO_2 is combined with highly conductive materials such as metal nanostructures [17], conducting polymers [18-21], graphene and carbon nanotubes [22- 27].

Because of a good chemical stability, high electric conductivity, large surface area, and unique architecture, graphene has been widely considered to be incorporated with MnO_2. Various approaches to synthesize MnO_2/graphene electrodes have been reported, including physical mixing, microwave-assisted method, chemical co-precipitation and electrochemical deposition [28, 29]. For instance, MnO_2/graphene electrodes synthesized by soft chemical route exhibited a specific capacitance (SC) of 210 Fg^{-1} [28] and those produced by microwave-assisted method displayed SC of 310 Fg^{-1} [29].

Compared to other methods for preparing MnO_2/graphene electrodes, electrochemical deposition is a green strategy that avoids using harsh chemicals (e.g. hydrazine) or high temperature treatment for reducing graphene oxide. In this regard, the electrochemical deposition method basically relies on electrophoretic deposition (EPD) technique in the processing of graphene-based ceramic, coating and composite materials from charged colloidal suspensions. In principle, the EPD technique has shown a number of advantages in the preparation of thin films such as high deposition rate, good thickness controllability and uniformity even on complex engineered surfaces such as three dimensional current collectors, cost effective and simplicity of scale up films with a good microstructure homogeneity and high packing density [27–32]. To synthesize MnO_2/graphene electrodes via electrophoretic deposition technique, either one of the following synthetic routes can be adapted; i) two steps route in which EPD-rGO being first assembled on a current collector template, shortly thereafter, the growth of nanoscale thin film of electrodeposited MnO_2 occurs, or, ii) one step route through which the coelectrophoretic deposition process occurs from stable suspensions containing both of MnO_2 and graphene or their precusors on current collector template [33].

This work is conclusively dedicated to develop MnO_2/graphene electrode via anodic deposition of nano-scale MnO_2 film on pre-electrophoretically graphene architecture coated on a three-

dimensional nickel foam conductive substrate. The MnO_2/graphene electrode will be characterized and exploited for supercapacitor application.

2. EXPERIMENTAL

Figure 1 shows a diagram of the single-compartment EPD cell experiment used to prepare graphene architecture on nickel foam substrate from colloidal suspensions of graphene oxide (GO). The GO used in this study was synthesized from purified natural graphite by the modified Hummers method [33]. The GO of typical concentration of 1.5 mg/mL was dispersed in water and sonicated for 0.5 h at room temperature. After the preparation of colloidal suspensions of individual GO platelets in purified water, the GO was deposited electrophoretically at applied voltage of 10 V on 3D nickel foam substrate of thickness 1.6 mm and surface area 1 cm^2.

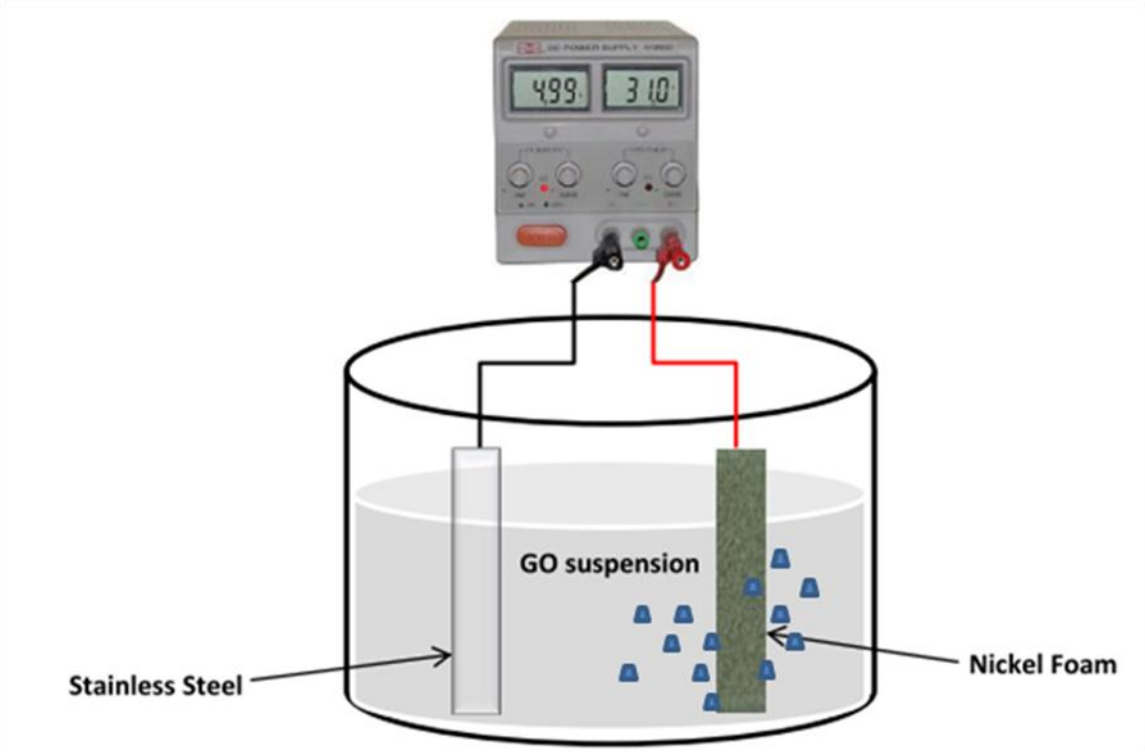

Figure 1. A single-compartment electrophoretic cell used to prepare EPD-rGO on nickel foam substrate from aqueous colloidal suspensions of GO.

After the deposition of EPD-rGO, a thin film of MnO_2 was deposited anodically at 1 V from 0.25 M $(CH_3COO)_2Mn.4H_2O$ solution using three electrode system with Ag/AgCl as a reference electrode (KCl saturated), Pt-wire as a counter electrode and the pre-prepared EPD-rGO/Ni foam as a working electrode. The mass loading of the MnO_2 is controlled by adjusting the total charge passed through the electrode during deposition process and selected to be 100 μg cm^{-2}.

The crystalline structure of the deposited films was characterized by means of X-ray diffractometer (Shimadzu, XRD-7000) using Cu Kα radiation. Raman spectroscopy and Fourier Transform Infrared spectroscopy (FT-IR) were used to characterize the structures of GO, EPD-rGO, and MnO_2/EPD-rGO using JASCO NRS-2100 Raman spectrometer with 514.5 nm wavelength incident laser light and FT-IR spectrophotometer (Perkin Elmer Spectrum BX II). The morphology of the deposited films was studied using a JEOL JSM-6360LA scanning electron microscope (SEM) and JEOL JEM-2010F transmission electron microscopy (TEM).

The electrodes have been tested in 0.5 M Na_2SO_4 electrolyte using three electrode configuration cell for electrochemical capacitor. The cyclic voltammetry (CV), galvanostatic charge–discharge, and electrochemical impedance spectroscopy (EIS) studies have been performed using VersaSTAT4 potenitostat/galvanostat electrochemical system.

The CV behaviors were carried out within a potential range of 0–0.9 V vs. Ag/AgCl (KCl saturated) at scan rates of 10–90 mV s^{-1}. Galvanostatic charge/discharge cycling was conducted at constant current densities of 1–10 mA cm^{-2} between 0–1 V. The cycle life test was performed at current density of 1 mA cm^{-2}. The applied alternating current amplitude for EIS measurements was 10 mV root mean square in a frequency range of 0.1 Hz to 100 kHz.

Cyclic voltammetry specific capacitance (C_{sp}) was calculated from dividing the capacitive charge (Q), obtained using half the integrated area of the CV curve, by the film mass (m) and the width of the potential window (V) using equation (1):

$$C_{sp} = \frac{Q}{m.V} \qquad (1)$$

Chronopotentiometry discharge specific capacitance C_{sp} values were calculated by using charge-discharge current (I), potential change with discharge time (dV/dt) and the mass of the deposited film according to the equation:

$$C_{sp} = \frac{I.dt}{m.dV} \qquad (2)$$

3. RESULTS AND DISCUSSION

3.1. Structure

Figure 2 compares the X-ray diffraction patterns of GO powder (a), and MnO_2 (b) and MnO_2/ EPD-rGO (c) films deposited on Ni-foam substrate. Compared to sharp reflection peaks emerge from nickel foam substrate and pristine GO (a), no obvious diffraction peaks can be observed in the patterns of MnO_2/EPD-rGO and/or MnO_2 films. This may refer to the transformation of GO by electrophoretic deposition to rGO. In addition, the deposited particles of MnO_2 are of such small size to have amorphous or poorly crystalline structures.

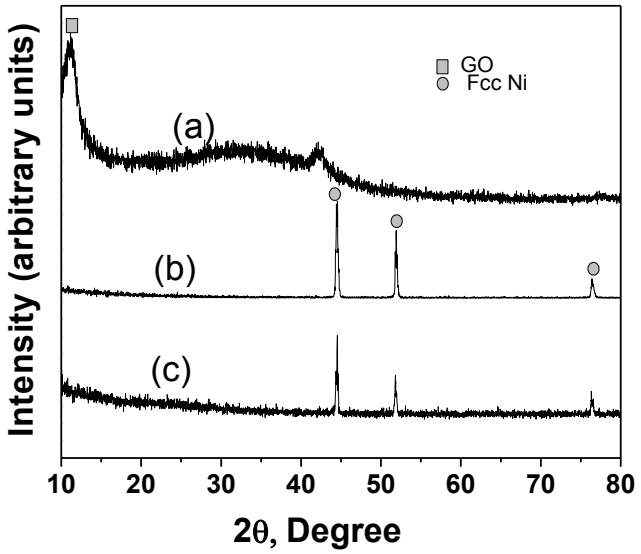

Figure 2. XRD patterns of GO powder (a), and MnO_2 (b) and MnO_2/EPD-rGO (c) films deposited on Ni-foam substrate

Figure 3 shows the FT-IR spectra of GO (a), EPD-rGO (b) and MnO_2/EPD-rGO (c). The FT-IR spectrum of the GO shows stretching vibration of several broad and intense peaks: a peak at 3412 cm^{-1} originates from O–H absorption, a peak at 1728 cm^{-1} is due to the C–O stretching of carboxylic groups placed at edges of GO sheets. Stretching vibration peaks of C–O (epoxy) and C–O (alkoxy) are observed at 1400 cm^{-1}, 1229 cm^{-1} and 1078 cm^{-1}, respectively. The peak at 1627 cm^{-1} corresponds to in plane C–C bonds and the skeletal vibration of the graphene sheets. On the other hands, FT-IR spectrum of EP-rGO (b), indicates that the electrophoretic deposition enables a complete removal of C=O (carboxylic), C–O (epoxy) and C–O (alkoxy) groups, partial elimination of hydroxyl groups along with simultaneous restoration of carbon-carbon bonding. It's worth mentioning that the remnants of hydroxyl groups are reported to be related to water molecules intercalated among graphene layers, which do not affect the hydrophobicity of graphene and usually improve electrical conductivity [35,36]. Also, the peak position of IR band related to the coupling mode between Mn-O stretching modes of tetrahedral and octahedral sites appears at 520 cm^{-1} in case of MnO_2/EPD-rGO deposited film instead of 574 cm^{-1} in the IR spectrum of the MnO_2 deposited film [37-39]. This reflects the formation of MnO_2/EPD-rGO hybrid film.

The structure within the EPD-rGO was also studied by Raman spectroscopy. Figure 4 presents Raman spectrum of carbon deposit in the MnO_2/EPD-rGO film. In general, the spectrum consist of three main bands typical characteristic of carbon material, a D-band at 1352 cm^{-1} and two overlapped bands appear at about 1580 and 1611 cm^{-1} assigned for G- and D′-bands, respectively [40-42]. The detected D-band is attributed to the defects due to the finite crystallite size or edges of graphene layers; while the G-band represents the in-plane bond-stretching motion of the pairs of carbon sp_2 atoms which indicates the presence of crystalline graphene layers.

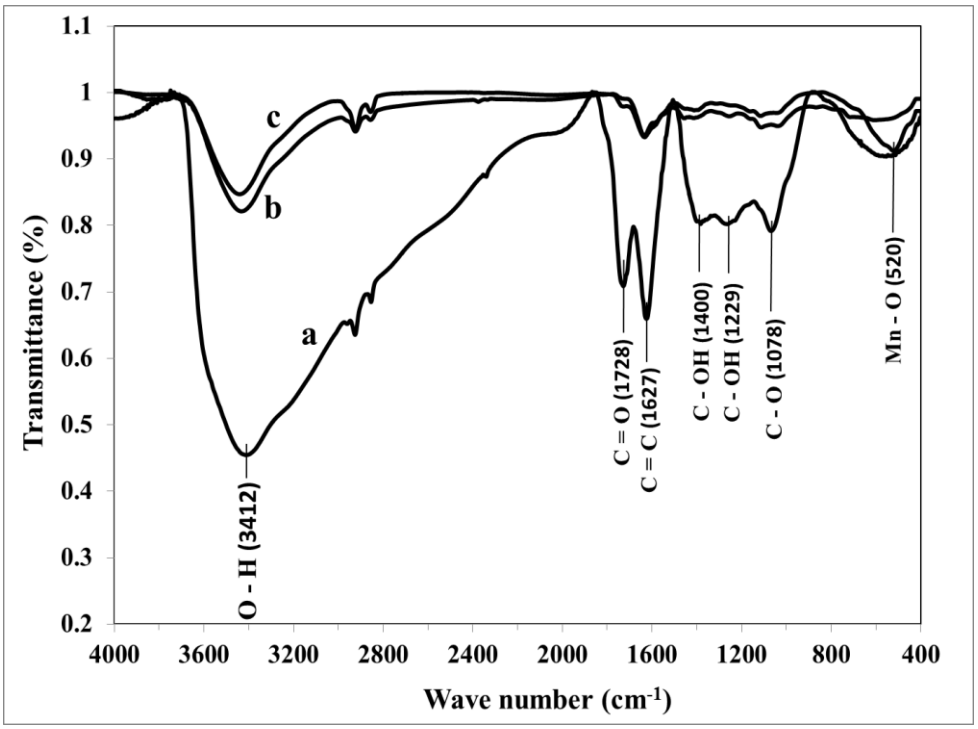

Figure 3. FT-IR spectra for of GO (a), EPD-rGO (b) and MnO_2/EPD-rGO (c).

The band corresponds to D′-band, indicating the disorder and associated with finite-size graphite crystals and graphene edges. In brief, the strong D-band peak and D′-band peak suggest presence of more nanocrystalline structure, graphene edges and defects such as distortion, vacancies and straining to graphitic lattices, which are prevalent features of disorder graphene [43-46]. It's worth to mention that the presence of defects and active edges in the graphitic lattices of carbon materials are prerequisites for supporting the nucleation and growth processes of the assembled electroactive nanoparticles and subsequently their service life.

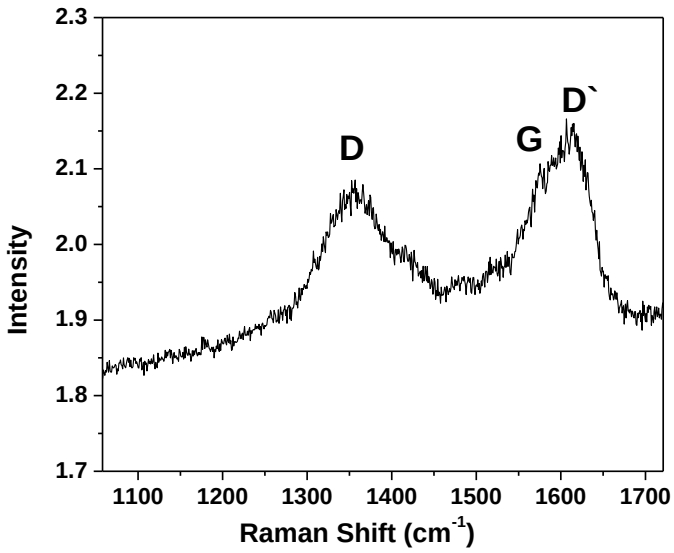

Figure 4. Raman spectrum of carbon deposit in the MnO_2/EPD-rGO film

3.2. Morphology

Figure 5 shows typical SEM images of MnO_2 (a), EPD-rGO (b) and MnO_2/EPD-rGO (c) films. While the electrodeposited MnO_2 film (a) shows smooth surface with continuous cracks due to drying shrinkage, the EPD-rGO film (b) shows overlapped platelets with crumpled morphology. Meanwhile, the anodcially deposited MnO_2 particles, Fig. 5(c), have partially grown as aggregates along graphene platelets, preferably on the energetically favorable sites such as defects and edges.

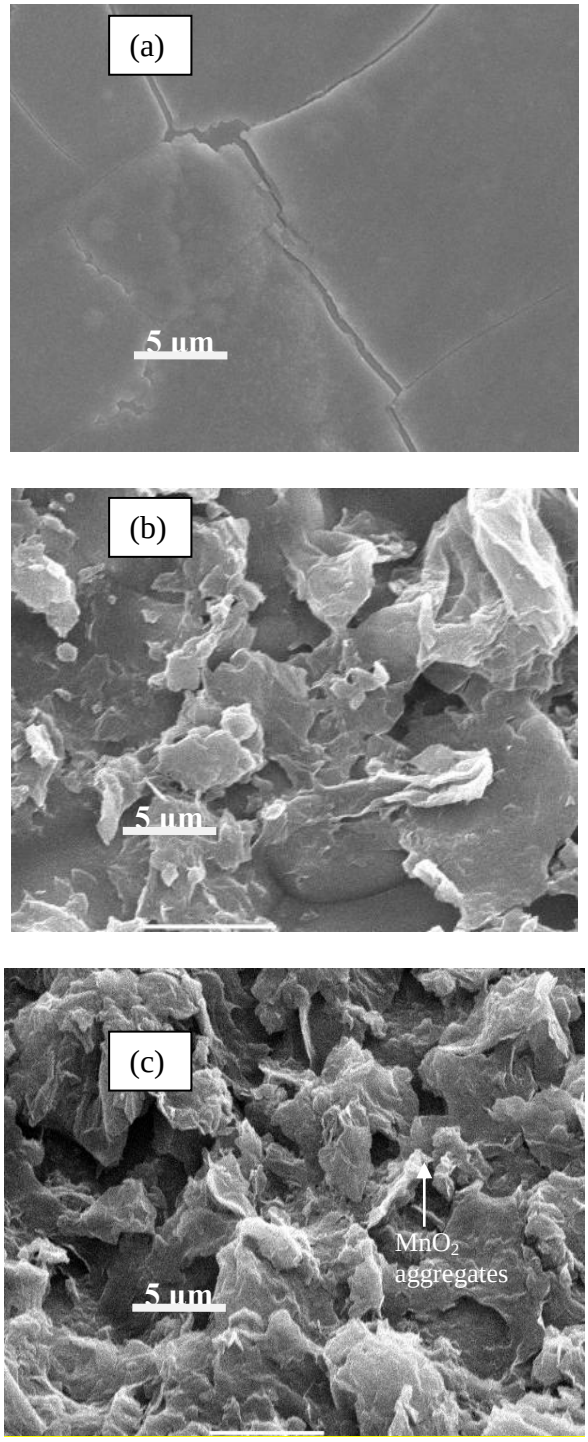

Figure 5. SEM images of MnO_2 (a), EPD-rGO (b) and MnO_2/EPD-rGO (c) films.

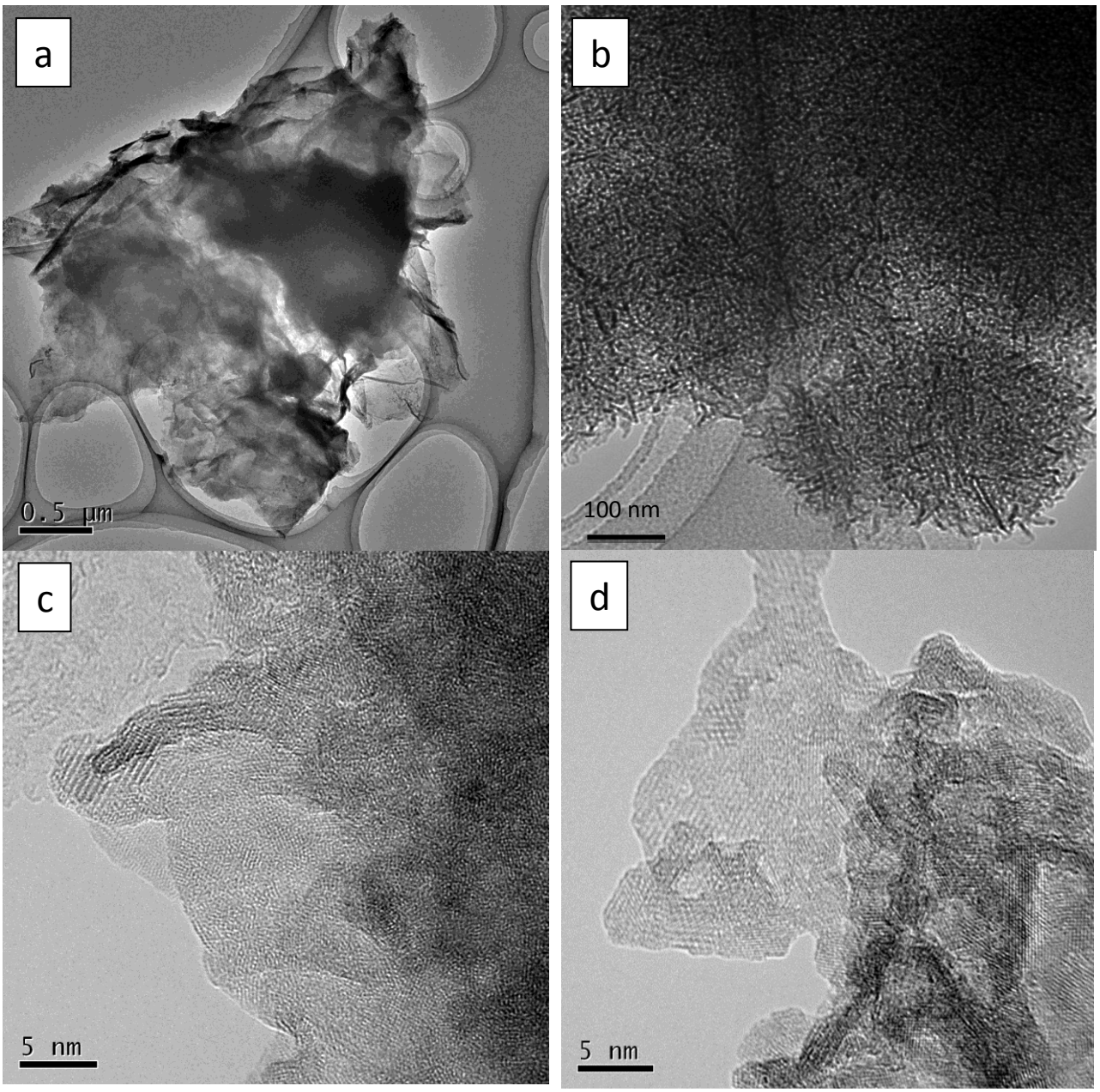

.

Figure 6. TEM images of MnO_2/EPD-rGO at different magnifications (a-c) and MnO_2-free EPD-rGO film (d).

Figure 6 shows TEM images of MnO_2/EPD-rGO film at different magnifications (a-c). The TEM image of MnO_2-free EPD-rGO film is also presented for comparison in Fig. 6(d). As seen in Figs. 6(a) and (b) thin film of flowers like MnO_2 is attached to the sheets of EPD-rGO film. In the images of Figs. 6 (c) and (d), the MnO_2 polymorph birnessite is clearly visible, while it tends to diminish in size and be less densely packed with the deposition on the EPD-rGO sheets. This means that the presence of underlying graphene leads to more efficient utilization and deposition of finer structure of nanocrystalline MnO_2. It's worth mentioning that the less closely packed and finer nanostructure phase of the oxide material are generally necessary to have mechanically stable and

conductive electrode with large surface area for supercapacitor applications due to easy penetration of ions through the bulk of the active material.

3.3. Electrochemical Supercapacitive Behavior

3.3.1. Cyclic Voltammetry (CV)

Figure 7 shows the CV comparison curves for bare nickel foam (a), EPD-rGO (b), MnO_2 (c) and the MnO_2/EPD-rGO (d) electrodes measured in 0.5 M Na_2SO_4 electrolyte at a scan rate of 90 mV s^{-1}. It is shown that the capacitive contributions of Ni foam (a) and EP-rGO (b) electrodes are negligible compared with those of MnO_2 (c) and the MnO_2/EPD-rGO (d) electrodes. The CV curves of MnO_2 (c) and the MnO_2/EPD-rGO (d) electrodes show nearly rectangular shape and characteristic mirror-image without clear redox peaks indicative of highly capacitive behaviour with good ion response. Meanwhile, the MnO_2/EP-rGO electrode shows the larger integrated area of the CV curve than that of MnO_2 electrode and hence, it has the highest C_{sp}.

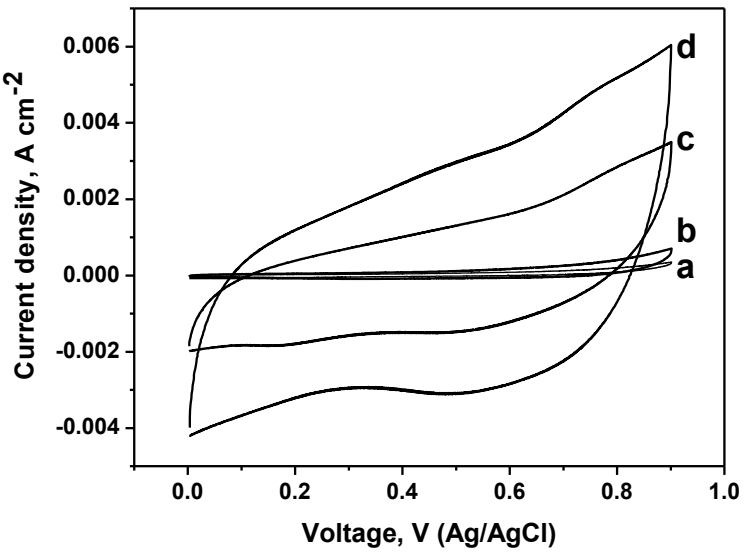

Figure 7. CV curves of bare nickel foam (a), EPD-rGO (b) EPD-rGO-free MnO_2 (c) and the MnO_2/EPD-rGO (d) electrodes measured in 0.5 M Na_2SO_4 electrolyte at a scan rate of 90 mV s^{-1}.

Figure 8 presents the variation in the specific capacitance with the scan rates for EPD-rGO (a), MnO_2 (b) and the MnO_2/EPD-rGO (c) electrodes. As seen, all electrodes show typical gradual decrease in the C_{sp} with the increase in the scan rate. The highest C_{sp} values for EPD-rGO (a), MnO_2 (b) and the MnO_2/EPD-rGO (c) electrodes at a scan rate of 10 mV s^{-1}, are 70, 488 and 617 Fg^{-1}, respectively. Hence, the presence of underlying EPD-rGO film provides more active sites for the redox reaction of manganese dioxide.

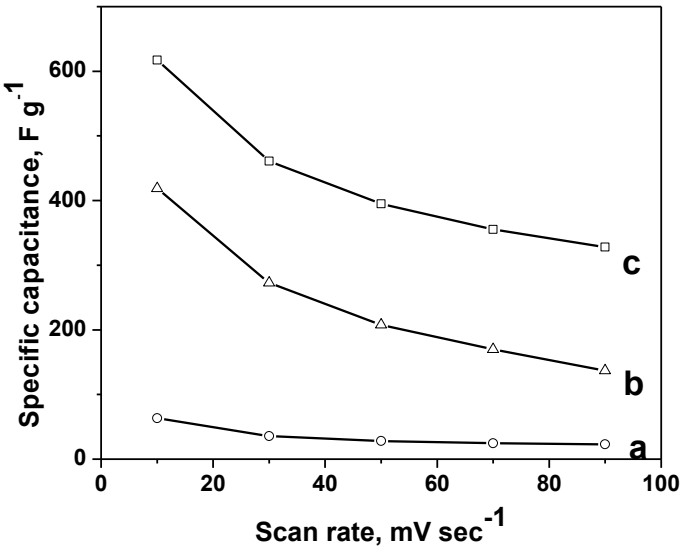

Figure 8. Variation of C_{sp} with the scan rate of CV measurements for EPD-rGO (a), MnO_2 (b) and the MnO_2/EPD-rGO (c) electrodes.

3.3.2. Galvanostatic charge-discharge characteristic and cyclic stability

To further clarify the effect of underlying EPD-rGO film on the capacitive behavior and rate capability of anodically deposited MnO_2 film, the charge-discharge profiles of all electrodes were measured by chronopotentiometry. Figure 9 shows charge-discharge profiles for EPD-rGO (a), MnO_2 (b) and the MnO_2/EPD-rGO (c) electrodes measured in 0.5 M Na_2SO_4 electrolyte at current density of 1 mA cm^{-2}. In principle, the discharge profile of any oxide film with capacitive characteristics is basically consisted of three parts: a resistive component from sudden voltage drop (IR drop) due to the internal resistance of the deposited film, the capacitance component related to the voltage change due to ion separation in the double layer region at the electrode interface, and finally faradaic component in the longer time region due to charge transfer reaction of the film. As can be seen, the IR drop for EPD-rGO (a), MnO_2 (b) electrodes are larger than that of MnO_2/EPD-rGO (c) electrode indicating that the MnO_2/EPD-rGO (c) film has lower internal resistance than those of EPD-rGO and MnO_2 films. After the initial voltage drop, the discharge curves of MnO_2 (b) and the MnO_2/EP-rGO (c) electrodes are nearly linear, indicating the capacitive and reversible behaviors of films. The MnO_2/EPD-rGO electrode has the highest C_{sp} as it has longer discharge time.

Figure 10 presents the summary plots of specific capacitance versus current density for MnO_2 (a) and the MnO_2/EPD-rGO (b) electrodes. In this figure, the discharge C_{sp} gradually decreases by applying high current density. The highest C_{sp} values obtained for MnO_2 and the MnO_2/EPD-rGO electrodes at current density of 1 mA cm^{-2} are 643 and 822 Fg^{-1}, respectively. This is in coincidence with the CV results presented in Figs. 7 and 8. The MnO_2/EPD-rGO electrode does not only show higher C_{sp} but also better capability rate of charge-discharge than MnO_2 electrode. It can, therefore, be said that EPD-rGO template provides more active sites for an efficient assembly and utilization of MnO_2 as promising pseudo-capacitance material.

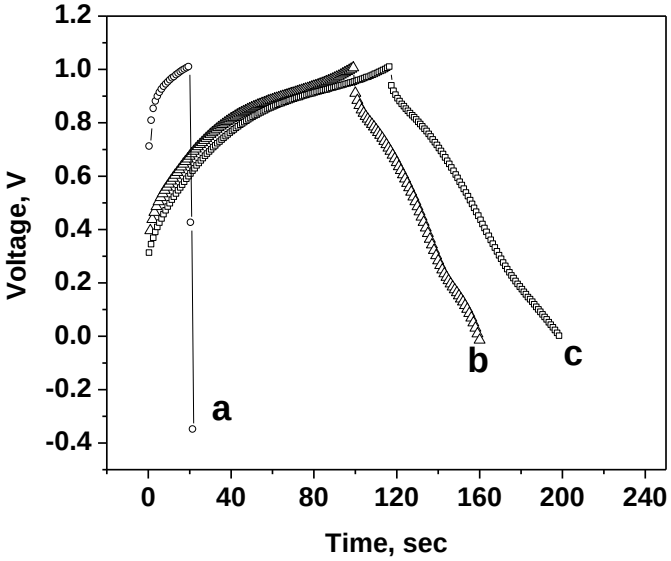

Figure 9. Charge-discharge curves for EPD-rGO (a), MnO_2 (b) and the MnO_2/EPD-rGO (c) electrodes in 0.5 M Na_2SO_4 electrolyte at a current density of 1 $mAcm^{-2}$.

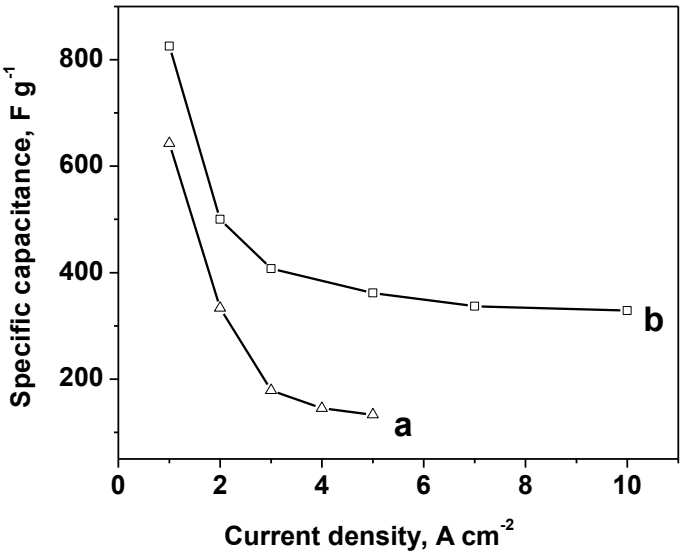

Figure 10. Variation of C_{sp} with discharge current density for MnO_2 (a), and MnO_2/EPD-rGO (b) electrodes.

Meanwhile, the charge-discharge test performed at current density 1 mA cm^{-2} for 1000 cycles revealed that the MnO_2 and MnO_2/EPD-rGO electrodes retained 61 and 89 % of their initial capacitances, respectively.

3.3.3. Electrochemical Impedance Spectroscopy

In order to understand the reason behind the unique capacitive performance of the MnO_2/EP-rGO electrode compared to MnO_2 electrode, a comparative electrochemical impedance spectroscopy

data were collected to quantify the electronic and ionic conductivities and diffusive behavior of the MnO_2-based films. Nyquist plots of as-prepared MnO_2 (a) and the MnO_2/EPD-rGO (b) electrodes were measured in 0.5 M Na_2SO_4 electrolyte over the frequency range from 100 mHz to 100 kHz as shown in Fig. 11. The Nyquist plots of MnO_2 (a) and the MnO_2/EPD-rGO (b) electrodes are closer to an ideal supercapacitor, which have a straight line in the low-frequency region and a small arc in the high frequency region. In principle, the very high-frequency intercept at the real impedance part (Z') at the beginning of the arc represents the equivalent series resistance (ESR) [47], which includes the ionic resistance of the electrolyte, the intrinsic resistance of the active material, intrinsic resistance of current collector, and the contact resistance at the interface between active material and current collector. The power density of supercapacitors depends strongly on the ESR [48]. The arc in the high-frequency region corresponds to the charge transfer resistance (R_{ct}) caused by the charge transfer process (Faradaic reactions) and double layer charging on the electrode surface. The magnitude of the R_{ct} can be derived from diameter of the arc [49]. The line at lower frequency region is a result of ion diffusion/transport from the electrolyte to the electrode surface [50]. The increasing slope trend of the line exhibits the capacitive nature related to the film charging mechanism that is the typical characteristic for porous electrodes.

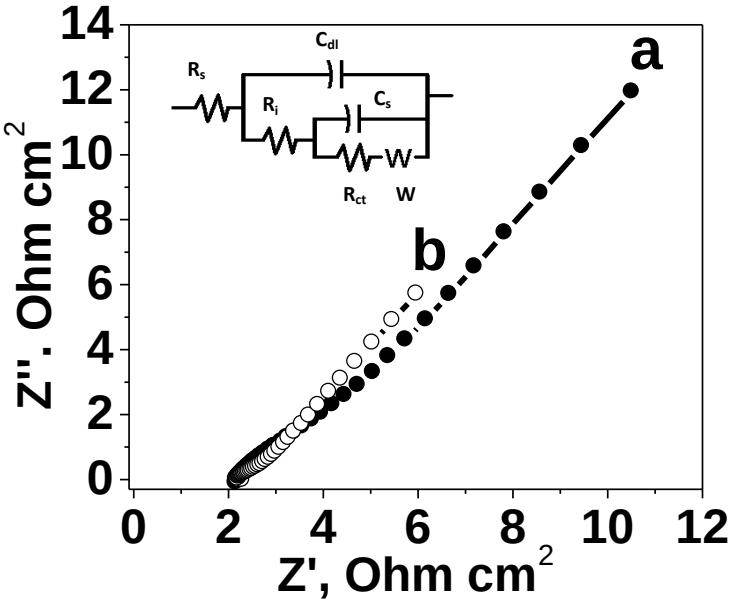

Figure 11. The high frequency region of the recorded full Nyquist plots for as prepared MnO_2 (a) and MnO_2/EPD-rGO (b) electrodes investigated in 0.5 M Na_2SO_4 electrolyte in the frequency range of 100 m Hz–100 kHz at 10 mV amplitude. The inset is the equivalent circuit proposed for the fitting of the impedance data.

The impedance data presented in Fig. 11 were analyzed using software provided with the electrochemical work station. The equivalent circuit model proposed for fitting the impedance data [20,24,25] is the inset of Fig.11. The model consists of R_s, solution resistance, R_i, interface resistance

which represents ESR value, R_{ct}, charge transfer resistance, W, Warburg impedance, C_{dl}, double layer capacitance, and C_s, pseudo-capacitance.

The fitting results show that the ESR values for MnO_2 and the MnO_2/EPD-rGO electrodes are 2.04 and 2.32 Ω, respectively. This refers that the contact resistance affects ESR with the presence of underlying EPD-rGO film compared with MnO_2 film. The R_{ct} values for MnO_2 and the MnO_2/EP-rGO electrodes are 3.28 and 0.52 Ω, respectively, reflecting the enhancement in the electronic and ionic conductivities of MnO_2 with the presence of underlying EPD-rGO film. Finally, the slope of the Nyquist plots in the low frequency region tends to increase with the presence of underlying EPD-rGO film (curve b) as compared with its absence (curve a), reflecting a decrease in the Warburg resistance (W) or fast electrolyte ion diffusion into the composite array.

In brief, the improvement in the capacitive performance of MnO_2 film is noticed with the presence of underlying EPD-rGO film. The presence of underlying EPD-rGO film creates more active sites, facilitates the access of the electrolyte ions onto the surface of MnO_2 and makes electron transport between underlying EPD-rGO film and MnO_2 easier as confirmed by the results obtained from EIS study. Finally, the energy density and power density values of MnO_2/EPD-rGO electrode estimated from the C_{sp} at charging-discharging current density of 1 mA cm^{-2} are 114 Wh kg^{-1} and 1077 W kg^{-1}, respectively.

4. CONCLUSIONS

We have demonstrated the successful preparation of MnO_2/EPD-rGO electrode via anodic deposition of amorphous MnO_2 film on pre-electrophoretically graphene architecture coated on a three-dimensional nickel foam substrate from aqueous solution of colloidally suspension GO. The FT-IR and Raman spectroscopy confirm that the EPD process enables the removal of oxygen functional groups of GO along with the formation of overlapped and stacked platelets of defective EPD-rGO sheets. The MnO_2/EPD-rGO electrode was characterized and exploited for supercapacitor application. It was found that the presence of underlying EPD-rGO film increased the capacitive behavior of the MnO_2 film. As the MnO_2/EPD-rGO electrode shows C_{sp} of 822 Fg^{-1} at current density 1 mA cm^{-2} and R_{ct} of 0.52 Ω. The MnO_2/EPD-rGO electrode exhibited energy density of 114 Wh kg^{-1} and power density of 1077 W kg^{-1}. The large surface area and defective nature of EPD-rGO film in conjunction with an efficient utilization of MnO_2 nanoparticles facilitated rapid ion transport and electrochemical cyclic stability, and hence offering the potential of the unique capacitive behavior for MnO_2/EPD-rGO electrode.

ACKNOWLEDGEMENTS

The authors gratefully acknowledge the Missions Sector-Higher Education Ministry, Egypt for financial support through this work and Materials Science and Engineering Department at E-JUST. Also we thank Mr. K. Hori and J. Koki of the Center for Advanced Material Analysis in Tokyo Tech. for assistance with TEM observations.

References

1. B.E. Conway, Electrochemical supercapacitors: scientific fundamentals and technological applications, Plenum Press, New York, 1999.
2. A. Burke, *Journal of Power Sources*, 91 (2000) 37-50.
3. P. Simon, Y. Gogotsi, *Nature materials*, 7 (2008) 845-854.
4. J.R. Miller, P. Simon, *Science*, 321 (2008) 651-652.
5. M. Inagaki, H. Konno, O. Tanaike, *Journal of Power Sources*, 195 (2010) 7880-7903.
6. A.A. El-Moneim, B.M. M., *International Journal of Electrochemical Science*, 7 (2012) 671 – 685.
7. A.A. El-Moneim, *International Journal of Hydrogen Energy*, 36 (2011) 13398-13406.
8. A.A. El-Moneim, J. Bhattarai, Z. Kato, K. Izumiya, N. Kumagai, K. Hashimoto, *ECS Transactions*, 25 (2010) 127-137.
9. A.A. El-Moneim, K. Kumagai, K. Hashimoto, *Materials Transactions*, 66 (2009) 1969-1977.
10. A.A. El-Moneim, N. Kumagai, K. Asami, K. Hashimoto, *Materials Transactions*, 46 (2005) 309-316.
11. K. Hashimoto, A.A. El-Moneim, N. Kumagai, K. Asami, *ECS Transactions*, 1 (2006) 491-497.
12. S. Hassan, M. Suzuki, A. Abd El-Moneim, *EEE Electrical and Electronic Engineering*, 2 (2012) 18-22.
13. S. Hassan, M. Suzuki, A. Abd El-Moneim, *American Journal of Materials Science*, 2 (2012) 11-14.
14. K. Hashimoto, M. Yamasaki, K. Fujimura, T. Matsui, K. Izumiya, M. Komori, A. El-Moneim, E. Akiyama, H. Habazaki, N. Kumagai, *Materials Science and Engineering*: A, 267 (1999) 200-206.
15. X. Zhao, B.M. Sanchez, P.J. Dobson, P.S. Grant, *Nanoscale*, 3 (2011) 839-855.
16. G.A. Snook, P. Kao, A.S. Best, *Journal of Power Sources*, 196 (2011) 1-12.
17. W. Wei, X. Cui, W. Chen, D.G. Ivey, *Chemical Society Reviews*, 40 (2011) 1697-1721.
18. L. Xingyou, H. Akihiko, F. Takeshi, C. Mingwei, *Nature Nanotechnology*, 6 (2011) 232-236.
19. L. Chen, L.-J. Sun, F. Luan, Y. Liang, Y. Li, X.-X. Liu, *Journal of Power Sources*, 195 (2010) 3742-3747.
20. S. Hassan, M. Suzuki, A.A. El-Moneim, *Journal of Power Sources*, 246 (2014) 68-73.
21. R. Liu, J. Duay, S.B. Lee, *ACS Nano*, 4 (2010) 4299-4307.
22. G. Yu, L. Hu, N. Liu, H. Wang, M. Vosgueritchian, Y. Yang, Y. Cui, Z. Bao, *Nano Letters*, 11 (2011) 4438-4442.
23. Z. Li, J. Wang, X. Liu, S. Liu, J. Ou, S. Yang, *Journal of Materials Chemistry*, 21 (2011) 3397-3403.
24. S. Hassan, M. Suzuki, S. Mori, A.A. El-Moneim, *Journal of Power Sources*, 249 (2014) 21-27.
25. S. Hassan, M. Suzuki, S. Mori, A.A. El-Moneim, *RSC Advances*, 4 (2014) 20479-20488.
26. J. Yan, Z. Fan, T. Wei, J. Cheng, B. Shao, K. Wang, L. Song, M. Zhang, *Journal of Power Sources*, 194 (2009) 1202-1207.
27. O.O. Van der Biest, L.J. Vandeperre, *Annual Review of Materials Science*, 29 (1999) 327-352.
28. J.F.Z.W.T.Q.W.Z.M.W.F. Yan, *Carbon Carbon*, 48 (2010) 3825-3833.
29. S. Chen, J. Zhu, X. Wu, Q. Han, X. Wang, *ACS Nano*, 4 (2010) 2822-2830.
30. P. Sarkar, P.S. Nicholson, *Journal of the American Ceramic Society*, 79 (1996) 1987-2002.
31. A.R. Boccaccini, I. Zhitomirsky, *Current Opinion in Solid State and Materials Science*, 6 (2002) 251-260.
32. M. Sawangphruk, P. Srimuk, P. Chiochan, A. Krittayavathananon, S. Luanwuthi, J. Limtrakul, *Carbon*, 60 (2013) 109-116.
33. Y.-Q. Zhao, D.-D. Zhao, P.-Y. Tang, Y.-M. Wang, C.-L. Xu, H.-L. Li, *Materials Letters*, 76 (2012) 127-130.
34. W.S. Hummers, R.E. Offeman, *Journal of the American Chemical Society*, 80 (1958) 1339-1339.
35. M. Wojtoniszak, X. Chen, R.J. Kalenczuk, A. Wajda, J. Łapczuk, M. Kurzewski, M. Drozdzik, P.K. Chu, E. Borowiak-Palen, *Colloids and Surfaces B: Biointerfaces*, 89 (2012) 79-85.

36. D. Li, M.B. Muller, S. Gilje, R.B. Kaner, G.G. Wallace, *Nat Nano*, 3 (2008) 101-105.
37. S. Karuppuchamy, J.M. Jeong, *Journal of Oleo Science*, 55 (2006) 263-266.
38. M. Ocaña, *Colloid & Polymer Science*, 278 (2000) 443-449.
39. C.M. Julien, M. Massot, C. Poinsignon, *Spectrochimica Acta Part A: Molecular and Biomolecular Spectroscopy*, 60 (2004) 689-700.
40. K. Tanaka, M. Yoshimura, A. Okamoto, K. Ueda, Japanese Journal of Applied Physics, 44 (2005) 2074-2076.
41. K. Kobayashi, M. Tanimura, H. Nakai, A. Yoshimura, H. Yoshimura, K. Kojima, M. Tachibana, *Journal of applied physics*., 101 (2007) 94306.
42. M.S. Dresselhaus, G. Dresselhaus, R. Saito, A. Jorio, *Physics reports*., 409 (2005) 47.
43. Y. Wu, P. Qiao, T. Chong, Z. Shen, *Advanced Materials*, 14 (2002) 64-67.
44. K. Shiji, M. Hiramatsu, A. Enomoto, M. Nakamura, H. Amano, M. Hori, *Diamond and Related Materials*, 14 (2005) 831-834.
45. Y. Wu, B. Yang, B. Zong, H. Sun, Z. Shen, Y. Feng, *Journal of Materials Chemistry*, 14 (2004) 469-477.
46. S. Mori, T. Ueno, M. Suzuki, *Diamond and Related Materials*, 20 (2011) 1129-1132.
47. Q. Lu, Y. Zhou, *Journal of Power Sources*, 196 (2011) 4088-4094.
48. A. Celzard, F. Collas, J.F. Marêché, G. Furdin, I. Rey, *Journal of Power Sources*, 108 (2002) 153-162.
49. T. Tüken, B. Yazıcı, M. Erbil, *Progress in Organic Coatings*, 50 (2004) 115-122.
50. M.D. Stoller, S. Park, Y. Zhu, J. An, R.S. Ruoff, *Nano Letters*, 8 (2008) 3498-3502.